

Cite this: *J. Mater. Chem. A*, 2020, **8**, 11155Received 18th February 2020  
Accepted 9th May 2020

DOI: 10.1039/d0ta01908a

rsc.li/materials-a

# Flexible fiber-shaped lithium and sodium-ion batteries with exclusive ion transport channels and superior pseudocapacitive charge storage†

Yalei Wang,<sup>a</sup> Yuanchuan Zheng,<sup>a</sup> Jiupeng Zhao <sup>\*a</sup> and Yao Li <sup>\*b</sup>

Fiber batteries have become increasingly important in the wearable energy market and thus, great efforts have been devoted to their development with better specific capacities, longer lifetimes, and sufficient flexibility. However, the sluggish kinetics of the ion transport in the electrochemical process has become a limitation for their practical applications. Herein, we directly employed 2D tungstate and graphene nanosheets as building blocks to construct fiber electrodes with 2D nanofluidic channels and 3D interconnected tunnels for exclusive and fast ion transport. These structures could accelerate the ionic transport process, avoiding the limitations from solid-state diffusion in the electrochemical process and finally facilitating efficient pseudocapacitive charge storage. The resulting fiber-shaped lithium- and sodium-ion batteries exhibited extremely high capacities (206 and 178 mA h g<sup>-1</sup> for LIBs and SIBs, respectively), excellent rate performance, long-term cycling capability (1000 cycles), and outstanding flexibility (200 bending cycles), which could continuously light an LED even under mechanical deformations. Thus, this work provides new insights into the structural engineering of fiber electrodes, showing great promise for boosting the battery performances in actual wearable applications to new levels.

## Introduction

Fiber batteries, one of the most advanced flexible energy storage systems, are making their way into the flexible electronics market.<sup>1–3</sup> With the growing popularity of wearable devices, the market is striving for batteries with better specific capacities, longer lifetimes, and better flexibility.<sup>4–8</sup> This race for

performance is usually focused on increasing the mass loading of active materials on the fiber substrates. However, this is undesirable since an overloaded electrode will inevitably impinge the flexibility, cause irreversible cracks in the active materials, and thus result in the inferior transport of electrolyte ions, which is at the expense of the overall performance.<sup>9–11</sup>

In practice, the sluggish kinetics of ion transport is generally identified as one of the main challenges for batteries to achieve desirable performances.<sup>12–14</sup> This limitation not only arises from the insertion/extraction kinetics within the active materials but also from the ion diffusion across the electrode, especially for overloaded fiber electrodes, because an increase in mass loading usually reduces the active surface areas and limits the electrolyte access to the bulky electrode. Therefore, processing the desired active materials into defined architectures, which is termed structural engineering, is expected to improve the kinetics of ion transport and enhance the battery performance. Since insertion/extraction is diffusion-controlled, employing active materials with an open host lattice is a great opportunity to accelerate ion transport.<sup>15–17</sup> For example, Clare P. Grey *et al.* employed niobium tungsten oxides that possessed an open crystalline structure as active materials, which demonstrated ion insertion/extraction rates far exceeding those of other typical materials.<sup>16</sup> Moreover, reducing the tortuosity of the ion path by aligned structures is an efficient method to expedite ion diffusion across the electrode.<sup>18–20</sup> As an example, André R. Studart *et al.* oriented graphite flakes to form an aligned structure in an electrode. The ion-path tortuosity of this oriented electrode was reduced by nearly four times, allowing the battery to be cycled at a fast rate up to 2C, with a specific capacity three times higher than that of the non-oriented electrode.<sup>19</sup> Inspired by the above-mentioned engineering framework strategies for conventional electrodes, new concepts based on the structural engineering of fiber electrodes will be promising but are still not explored completely.

With the development of 2D nanomaterials, tungstate nanosheets (Cs<sub>4</sub>W<sub>11</sub>O<sub>36</sub><sup>2-</sup>) have been recently considered as

<sup>a</sup>MIIT Key Laboratory of Critical Materials Technology for New Energy Conversion and Storage, School of Chemistry and Chemical Engineering, Harbin Institute of Technology, Harbin 150001, China. E-mail: jpzhaoh@hit.edu.cn

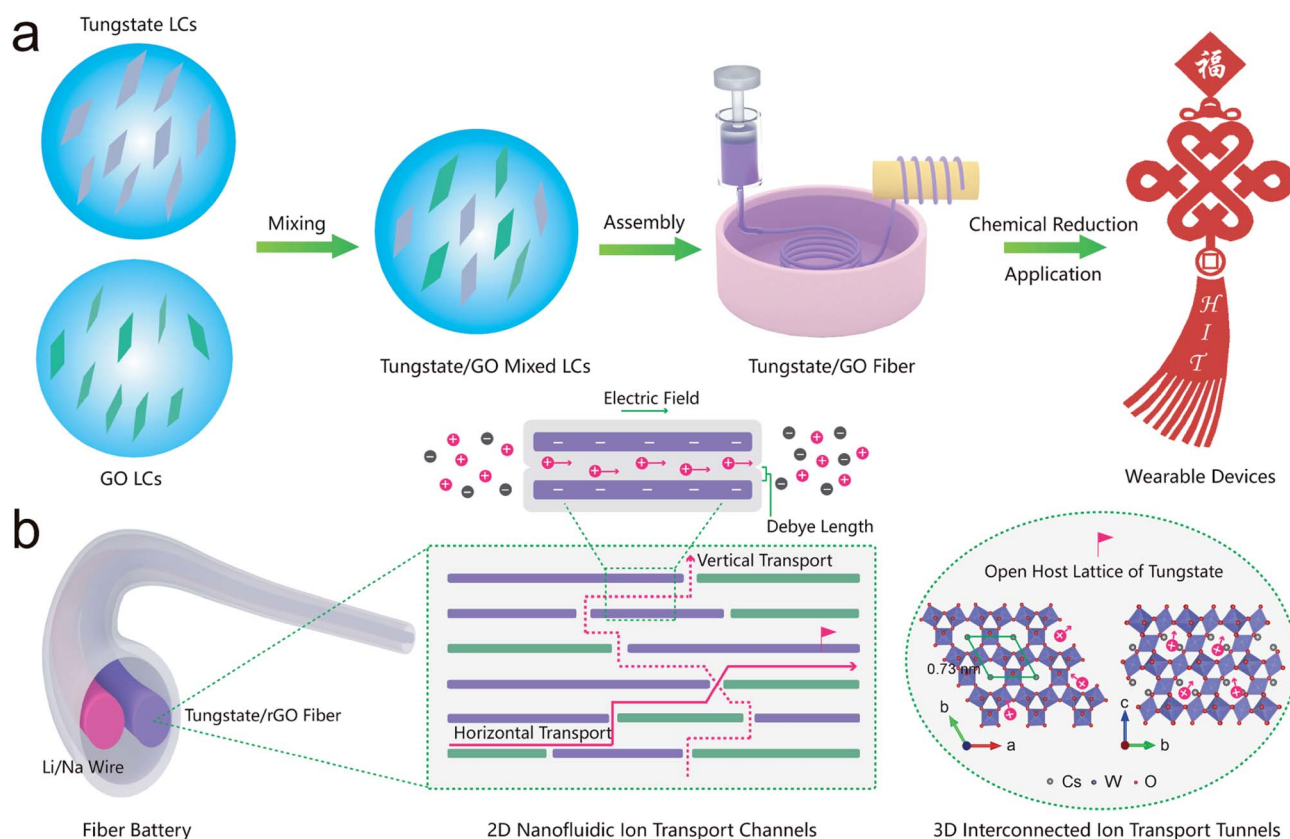
<sup>b</sup>Center for Composite Materials and Structure, Harbin Institute of Technology, Harbin, 150001, China. E-mail: yaoli@hit.edu.cn

† Electronic supplementary information (ESI) available. See DOI: 10.1039/d0ta01908a

promising active materials for fast ion transport because of their superlattice of hexagonal tunnels by  $\text{WO}_6$  octahedra chains.<sup>21,22</sup> The rigid, open, and 3D interconnected tunnel structures can be proposed as metaphorical multi-lane highways for ion transport, enabling intercalated ions to change their path and move through the active material in three dimensions without being trapped and much more quickly. Moreover, tungstate nanosheets possess an ultrathin 2D structure with a thickness on the molecular scale and lateral size in the order of micrometers, which can also shorten the ion diffusion distance and result in extra charge storage sites due to their large exposed surfaces.<sup>23,24</sup> Also, their huge 2D anisotropy (lateral size *versus* thickness) endow them potential to serve as building blocks for macroscopic fiber assembly, facilitating the design and fabrication of aligned structures.<sup>25,26</sup> More importantly, benefitting from the inherent negative surface charge of the nanosheets, 2D nanofluidic ion transport channels can be achieved by controlling the stacked spacing to be comparable to the double-Debye length of the electrolyte ion. The negatively charged channels will enable unipolar transport for the positive electrolyte ions and enhance the ionic conductivity up to several magnitudes, holding great promise to improve the ionic transport property in fiber batteries.<sup>27-29</sup>

Accordingly, herein, we employed 2D tungstate nanosheets as the major building-blocks to fabricate a structural electrode for fiber batteries through a scalable wet-spinning technique, as

illustrated in Scheme 1a. Subsequently, the aligned stacking structures were obtained *via* a macroscopic assembly process due to the long-range ordering of a mixed liquid crystal (LC) colloid. Based on the cooperation of stacked spacing and negative surface charge, 2D nanofluidic ion transport channels (horizontal and vertical) were achieved, as shown in Scheme 1b. An electrostatic field could be formed and maintained based on the overlapping Debye layers in the channels, which repelled the negative ions and attracted positive ions, making the positively charged electrolyte ions the dominating charge carriers, thereby minimizing the ion-path tortuosity and accelerating the ion diffusion process greatly. Moreover, profiting from the open host lattice, the intercalation ions could realize fast and efficient transport without limitations from solid-state diffusion in the 3D interconnected ion transport tunnels, delivering superior pseudocapacitive charge storage (inset in Scheme 1b). As expected, the designed tungstate/rGO fibers exhibited a high specific capacity, excellent rate performance, and long-term cycling lifetime for both a fiber-shaped lithium-ion battery (LIB) and sodium-ion battery (SIB). Meanwhile, due to the interstratified stacking structures within the fibers, all the fiber batteries exhibited outstanding flexibility, which could effectively retain the above electrochemical features even under mechanical deformations. This work highlights the significance of structural engineering for fiber electrodes and presents new insights to build practical fiber batteries.



**Scheme 1** Structural engineering of the fiber electrode based on 2D tungstate nanosheets. (a) Processing route from 2D tungstate nanosheets to the structural fiber electrode. (b) Schematic illustration of ion transport within the structural fiber electrode.

## Structure and morphology of 2D tungstate nanosheets

The tungstate nanosheets possess a molecular ultrathin 2D structure (theoretical thickness of 1.83 nm) due to the exfoliation of the layered tungstate crystals. As shown in Fig. 1a, the open host lattice is composed of connected  $\text{WO}_6$  octahedra with corner-sharing configurations, forming hexagonal 3D interconnected tunnels that are held open by cesium pillars. According to the transmission electron microscopy (TEM) image (Fig. 1b), the homogeneous and almost transparent contrast also reveals their ultrathin 2D structure. Also, the high-resolution transmission electron microscopy (HRTEM) image clearly shows the open hexagonal lattice tunnels of the  $\text{WO}_6$  octahedra in the nanosheets (Fig. 1c). All the diffraction spots in the corresponding selected area electron diffraction (SAED) pattern can be indexed well to a hexagonal lattice with  $a = 0.73$  nm (Fig. 1d), consistent with the known length of the Cs–Cs bond (inset in Scheme 1b). This result confirms that the host lattice structures are held open by the cesium pillars, showing great promise for fast ion transport. According to the atomic force microscopy (AFM) images (Fig. 1e and f), the nanosheets exhibit an average thickness of about 2.0 nm, which is consistent with the theoretical thickness of monolayer tungstate nanosheets. Owing to its huge 2D anisotropy ratio (lateral size *vs.* thickness of over 600) and excellent dispersibility, the tungstate nanosheet colloid exhibited distinctive LC behaviors. As shown in the polarizing optical microscopy (POM) image (Fig. 1i), vivid interference colors and Schlieren textures can be

observed, which are evidence of the formation of the LC phase, suggesting the presence of long-range ordering in the nanosheets. Consequently, the tungstate LC colloid can be directly employed for macroscopic fiber assembly through a wet-spinning process, similar to the fabrication of graphene fibers from GO LC colloid.<sup>25,26</sup>

## Macroscopic assembly of fiber electrode

Considering the unsatisfactory electroconductivity of the tungstate nanosheets, the introduction of a conductive component is necessary. Accordingly, graphene is an ideal partner to construct fiber electrodes due to its similar 2D geometric configuration and good conductivity. The GO colloid was synthesized *via* an improved Hummer's method.<sup>30</sup> As shown in the AFM images, the GO nanosheets also possess an ultrathin 2D structure with an average thickness of about 0.8 nm (Fig. 1g and h). Similarly, the GO colloid also showed LC behaviors under POM observation (Fig. 1j). In particular, because of the same negative surface charge (zeta potential in Fig. S1†), the tungstate and GO LC colloids could be mixed uniformly without precipitation, as shown in the inset of Fig. 1k. This stable and homogenous mixture colloid also exhibited similar LC behavior, which suggests the presence of a long-range ordering structure in the mixed nanosheets, enabling them to serve as collaborative building-blocks for the construction of fiber electrodes. Accordingly, tungstate/rGO fiber was fabricated *via* an industrial wet-spinning technique

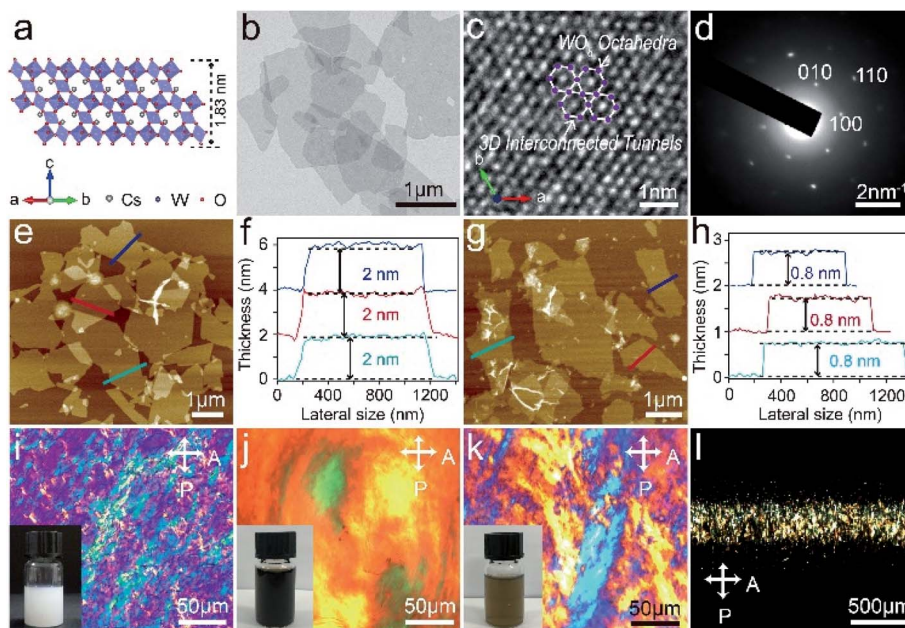


**Fig. 1** Structure and morphology characterization of the tungstate and GO nanosheets. (a) Crystal structure of the tungstate nanosheets along the (110) direction. (b) TEM image. (c) HRTEM image and (d) corresponding SAED diffraction pattern of the tungstate nanosheets. (e) Typical AFM image and (f) height profiles of the tungstate nanosheets. (g) Typical AFM image and (h) height profiles of GO. (i) POM images of tungstate nanosheet LCs, (j) GO LCs, and (k) tungstate/GO mixed LCs under crossed polarizers. The inset is the corresponding digital photographs of these LC colloids, respectively. (l) POM image of tungstate/GO mixed LCs induced by shear stress. P and A represent the directions of the polarizer and analyzer, respectively.

using the mixed LC colloid, followed by a chemical reduction (Scheme 1a). In this process, the LC domains oriented along the direction of the uniaxial spinning channel upon shear flow. As shown in Fig. 11, the homogeneous birefringence textures in the channel evidence the long-range ordering of the nanosheets, which provide a foundation for the macroscopic fiber assembly. Next, aligned “brick-and-mortar” stacking structures were achieved within the fiber when the LC colloid was injected into a coagulating bath of protonated chitosan, which is composed of the “bricks” of tungstate/rGO nanosheets and the “mortar” of chitosan molecules. Finally, after chemical reduction in hydroiodic (HI) acid, the oxygenated groups on GO were eliminated to form conductive networks, while the chitosan molecules were removed to produce vacant stacking spacing for ion transport.

## Structure analysis of the fiber electrode

The scanning electron microscopy (SEM) images for the tungstate/GO fiber show a crumpled surface morphology with a width of  $\sim 200 \mu\text{m}$  (Fig. S2†). After reduction, the resulting tungstate/rGO fiber also exhibited a similar morphology without any obvious cracks or defects (Fig. 2a and b, respectively). Note that both fibers exhibited a bright birefringent color under POM observation, suggesting an aligned structure

within the fibers (Fig. S3†). Moreover, as shown in the cross-sectional SEM images (Fig. 2c and d), the tungstate/rGO fiber exhibited an aligned inner structure, which confirms that the long-range ordering from the LC colloid was successfully inherited during the fabrication. In the HRTEM image of the tungstate/rGO fiber cross-section (Fig. 2e), interstratified stacking structures can be observed, which offer direct structural information on the assembly of the tungstate and rGO nanosheets, suggesting molecular hybridization of each other. As mentioned above, 2D nanofluidic channels were established *via* the collaboration of appropriate stacking spacing and surface charge. The theoretical stacking distance ( $D_t$ ) can be estimated based on the Debye length of the electrolyte ion ( $\lambda_D$ , unit in meters), which can be calculated as follows:

$$D_t = 2 \times \lambda_D = 2 \times \frac{3.04 \times 10^{-10}}{Z_i \sqrt{C_i}} \quad (1)$$

where  $Z_i$  and  $C_i$  denote the valency and concentration of electrolyte ions (i), respectively. For the electrolyte ( $\text{LiPF}_6$ , 1 M) of LIBs and electrolyte ( $\text{NaClO}_4$ , 1 M) of SIBs used in this work, the corresponding theoretical distance is 0.6 nm.<sup>31,32</sup> The actual stacking spacing between the nanosheets was measured by HRTEM. Fig. 2f displays the distance profile for the five-layer stacked nanosheets. The average interlayer distance ( $D_a$ ) was calculated using the difference between total stacked distance

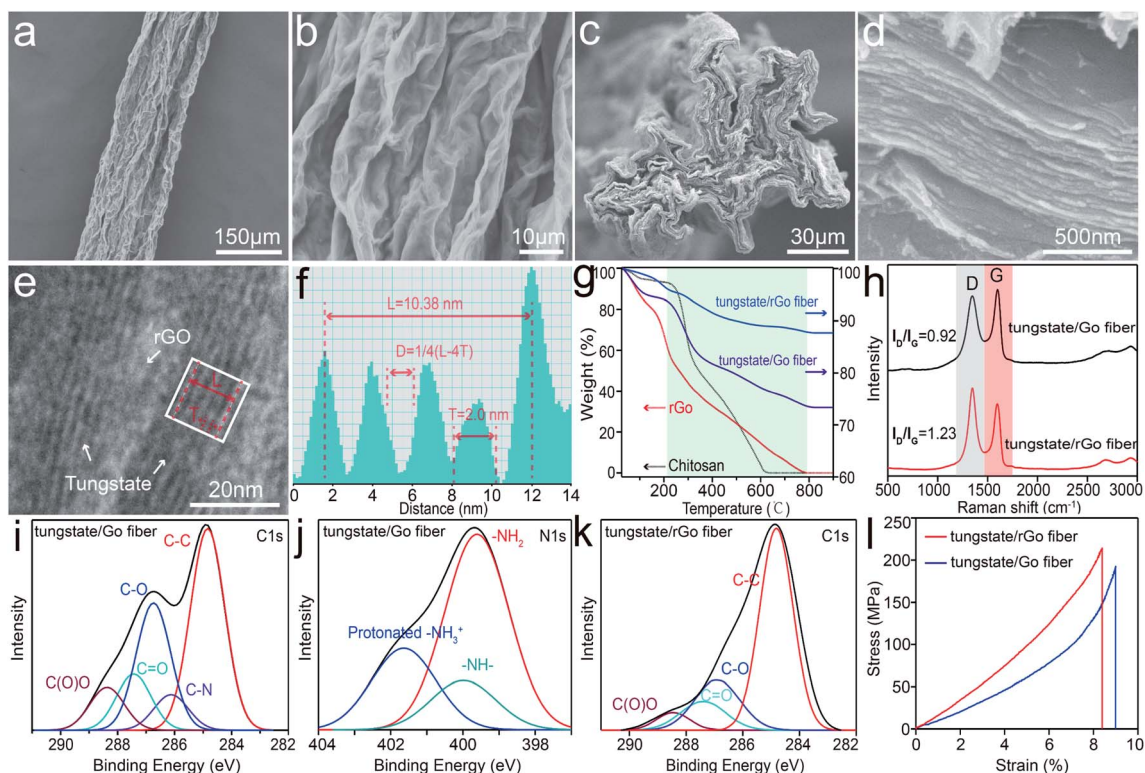


Fig. 2 Structure analysis for the fiber electrode. (a and b) SEM images of the tungstate/rGO fiber at different magnifications. (c and d) Cross-sectional SEM images of the tungstate/rGO fiber at different magnifications. (e) Cross-sectional HRTEM image of the tungstate/rGO fiber. (f) Corresponding interlayer distance profiles of the stacked nanosheets in e. (g) TGA analysis of rGO, chitosan, tungstate/GO fiber, and tungstate/rGO fiber. (h) Raman spectra of tungstate/GO fiber and tungstate/rGO fiber. (i and j) High-resolution XPS spectra of C 1s and N 1s for the tungstate/GO fiber. (k) High-resolution XPS spectra of C 1s for the tungstate/rGO fiber. (l) Typical mechanical tensile curves of the tungstate/GO fiber and tungstate/rGO fiber.

( $L = 10.38$  nm) and the thickness of stacked nanosheets (single layer thickness ( $T$ ) is 2.0 nm), as follows.

$$D_a = \frac{L - 4T}{4} \quad (2)$$

Therefore the interlayer distance between the stacked nanosheets is about 0.595 nm, which corresponds to the theoretical value. Combined with the intrinsic negative surface charge of the tungstate nanosheets, 2D nanofluidic ionic transport channels were achieved, which allow unipolar transport for positive  $\text{Li}^+$  and  $\text{Na}^+$ , providing a shorter diffusion pathway for them across the fiber electrode.

After chemical reduction, the removal of chitosan and the content of rGO in the tungstate/rGO fibers were investigated *via* thermogravimetric analysis (TGA). As shown by the green zone in Fig. 2g, the weight loss was mainly caused by the thermal decomposition of chitosan before 600 °C and pyrolysis of rGO before 800 °C. The thermal combustion stage of the tungstate/rGO fiber (blue line) was significantly shorter compared with that of the tungstate/GO fiber (purple line), which demonstrates the successful removal of chitosan after reduction. According to the analysis and comparison of the thermogravimetric curves for rGO (red line) and the tungstate/rGO fiber (blue line) and considering the weight loss of water, the content of rGO in the tungstate/rGO fiber was estimated to be 9.7 wt%. Moreover, the reduction of GO in the fiber was also surveyed by Raman spectroscopy, as shown in Fig. 2h. The D band arising from the disorder in the  $\text{sp}^2$ -hybridized carbon and the G band arising from the stretching of the C–C bond were observed for the fibers. After the reduction, the intensity ratio of the D band to G band ( $I_D/I_G$ ) increased from 0.92 to 1.23, suggesting the successful reduction of GO in the tungstate/rGO fiber. Combined with energy-dispersive spectroscopy (EDS) mapping of the tungstate/rGO fiber (Fig. S4†), the carbon element from rGO was observed to be uniformly distributed over the whole fiber, which can serve as a conductive network during the electrochemical process.

X-ray photoelectron spectroscopy (XPS) was also employed to investigate the hybridization between the tungstate and rGO nanosheets. For the tungstate/GO fiber, the C 1s spectra (Fig. 2i) could be fitted into five peaks of C–C (284.7 eV), C–N (286.3 eV), C–O (286.9 eV), C=O (287.4 eV), and C(O)O (288.6 eV), respectively. Also, the N 1s spectra could be fitted into three peaks of  $-\text{NH}_2$  (399.4 eV),  $-\text{NH}$  (400.0 eV), and  $-\text{NH}_3^+$  (401.8 eV), respectively (Fig. 2j). These results suggest that the negatively charged tungstate and GO nanosheets in the tungstate/GO fiber are coupled with each other by electrostatic interactions *via*  $-\text{NH}_3^+$  of the protonated chitosan. After chemical reduction, the peak of C–N located at 286.3 eV in the C 1s spectra (Fig. 2k) and the feature peak of N element located at about 400 eV in the survey spectrum (Fig. S5†) disappeared, evidencing the removal of chitosan in the tungstate/rGO fibers. Moreover, the C–C peak exhibited a strong intensity, while the C–O, C=O, and C(O)O peaks were weakened remarkably, and the ratio of O to C element decreased from 0.95 to 0.35, demonstrating the successful elimination of oxygen-containing functional groups

in GO. Additionally, the high-resolution XPS spectra of W 4f for both the tungstate/GO and tungstate/rGO fibers exhibited doublet components at 37.7 and 35.6 eV, which can be associated with the splitting orbits of W  $4f_{5/2}$  and W  $4f_{7/2}$ , respectively, and the spin–orbit separation is 2.1 eV, suggesting that the W atoms are in the +6 valence state (Fig. S6†). Also, no obvious changes could be found in the XRD patterns of the tungstate/GO and tungstate/rGO fibers (Fig. S7†). Thereby, the chemical reduction process did not influence the 2D tungstate nanosheets as the major component in the aligned stacking structures, and the surface charges of the tungstate remained intact in the chemical reaction process. In the interstratified stacking structures, the reduction of GO was accompanied by the restoration of the  $\pi$ – $\pi$  conjugation, inducing a more powerful sheet-to-sheet binding interaction within the tungstate/rGO fibers. It was expected that the strong sheet interaction should keep the aligned stacking structures intact after the removal of protonated chitosan and improve the mechanical properties of the fibers. As shown in Fig. 2l, the tungstate/rGO fiber exhibited a stronger tensile strength than the tungstate/GO fiber, which could reach about 210 MPa, satisfying the aim for it to serve as a flexible fiber electrode.

## Fiber-shaped lithium-ion battery

To evaluate the electrochemical performance of the fibers, fiber-shaped LIBs were assembled with the tungstate/rGO fibers and Li wire in parallel (details in the Experimental section). As shown in Fig. S8,† the galvanostatic charge/discharge curves at different cycles display the capacity profiles for the tungstate/rGO fibers with a length of 8 cm at 0.052 mA. The initial charge and discharge capacities were 215.4 and 261.2  $\text{mA h g}^{-1}$ , respectively, yielding an initial coulombic efficiency (CE) of 82.5%. This irreversible capacity loss should be ascribed to the formation of a solid-electrolyte interphase (SEI) layer on the electrode/electrolyte interface. After ten charge/discharge cycles, the reversible capacity was maintained at 206.3  $\text{mA h g}^{-1}$  with a CE of  $\sim 100\%$ , which exhibits a tiny capacity loss compared to the initial capacity, suggesting the high reversibility of the fiber. As shown in Fig. 3a, the galvanostatic charge/discharge curves display a continuous reduction in voltage with an increase in discharge capacity and without a distinct voltage plateau, which suggest a fast  $\text{Li}^+$  intercalation process without phase transformations. Even under the high current of 0.52 mA, the reversible capacity could still be maintained at 134.5  $\text{mA h g}^{-1}$ . More importantly, when the current decreased to 0.052 mA again, the reversible capacity returned to its initial value with a CE of  $\sim 100\%$  (Fig. 3b), indicating the excellent rate capability of the fibers. Fig. 3c displays the long-term cycling performance of the fiber battery. The reversible capacity under 0.52 mA was 170  $\text{mA h g}^{-1}$  in the initial cycle and was still maintained as high as 137.9  $\text{mA h g}^{-1}$  even after 1000 cycles with a CE of  $\sim 100\%$ , much higher than that for the pure tungstate (Fig. S9†). The high capacity retention (81.1%) proves that the tungstate/rGO fiber possesses superior long-term cycling stability during fast and continuous  $\text{Li}^+$  intercalation. To better understand the excellent

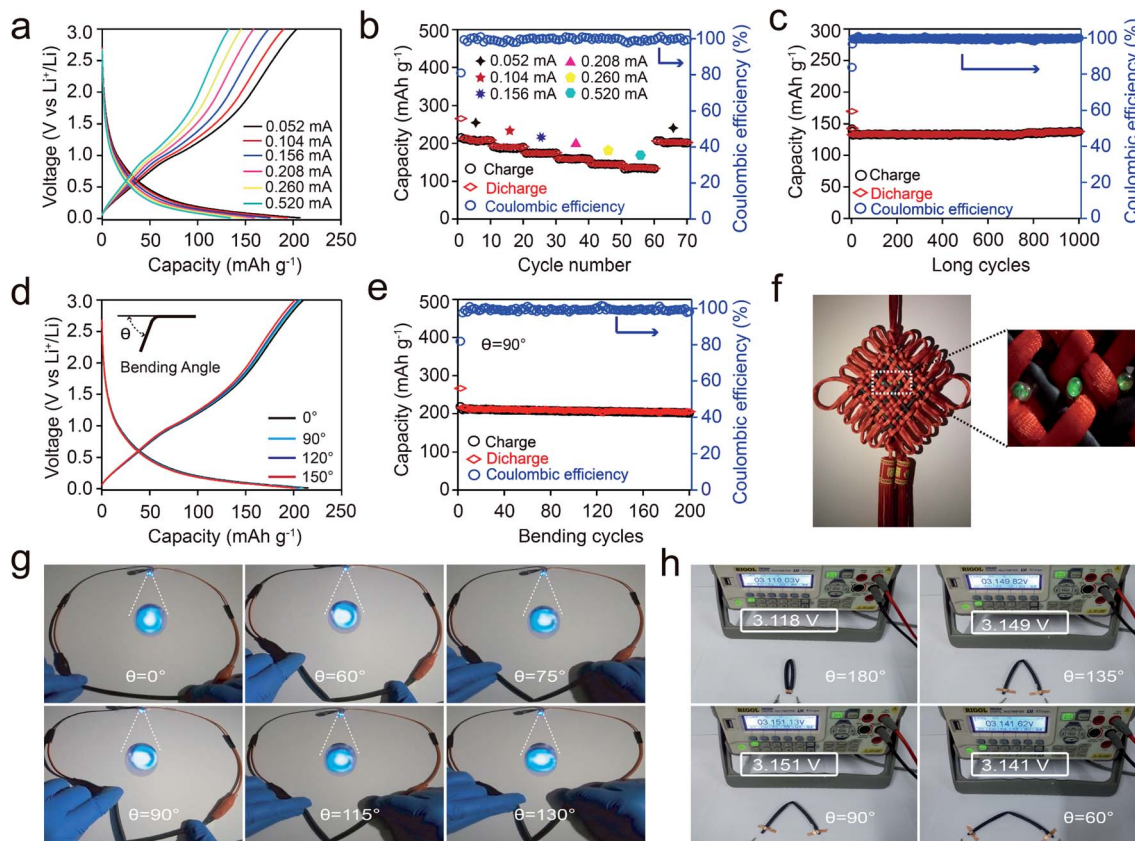


**Fig. 3** Electrochemical performance of fiber-shaped LIBs. (a) Galvanostatic charge/discharge profiles of the fiber battery under different currents ranging from 0.052 to 0.520 mA. (b) Rate capability of fiber battery under different currents ranging from 0.052 to 0.520 mA. (c) Cycling performance and corresponding coulombic efficiency of the fiber battery at 0.520 mA. (d) Galvanostatic charge/discharge profiles of the fiber battery under different bending angles at 0.052 mA. (e) Bending cycling performance of fiber battery under a bending angle of 90° at 0.052 mA. (f) Photographs of the fiber batteries woven into a Chinese knot and lighting three green LEDs. (g) Photographs of a fiber battery lighting a blue LED under different bending angles. (h) Voltage outputs of the fiber battery under different bending angles.

electrochemical performances of the tungstate/rGO fiber, the impedance of the fiber electrode was investigated (Fig. S10†). The Nyquist plot consists of a straight line in the low frequency region and a semicircle in the high frequency region, exhibiting a small equivalent series resistance ( $R_s$ ) and charge-transfer resistance ( $R_{ct}$ ). The  $R_s$  value was about 78.9  $\Omega$ , which decreased to about 47.4  $\Omega$  after 100 cycles. The  $R_{ct}$  value was about 277.3  $\Omega$  and decreased to about 124.1  $\Omega$  after 100 cycles. This phenomenon can be attributed to the interstratified stacking structures of tungstate and graphene, which facilitated pathways for lithium ions and charge transfer once the system was stabilized, resulting from the exclusive 2D nanofluidic ion transport channels, fast 3D interconnected ion transport tunnels, and excellent conductive networks of the conformal stacking graphene. Meanwhile, the large slope of the straight line in the low-frequency zone suggests low Warburg impedance and good ion diffusion in the fiber. As a result, the tungstate fiber exhibited excellent electrochemical performances.

The superiority of the fiber in the charge-storage kinetics was further analyzed *via* a cyclic voltammetry (CV) experiment. As shown in Fig. S11a,† the CV curves display similar broad redox peaks with small voltage offsets and increasing current with an increase in the scan rate. The power-law relationship between

the peak current ( $i$ ) and scan rate ( $\nu$ ) can be utilized to analyze the charge-storage mechanism, which obeyed the following relation:

$$i = a \times \nu^b \quad (3)$$

where  $a$  and  $b$  are constants. Also, the  $b$  values of 0.5 and 1 indicate a semi-infinite linear diffusion process and capacitive-controlled charge storage, respectively, which can be determined by the slope of the  $\log(i)$  versus  $\log(\nu)$  plot.<sup>33,34</sup> As shown in Fig. S11b,† the  $b$  values for anodic and cathodic peaks were calculated to be approximately 0.91 and 0.95, respectively, suggesting the charge storage should be dominated by a capacitive process. The capacitive contribution to the current at a certain scan rate can be quantitated by separating the current response ( $i$ ) from the capacitive ( $k_1\nu$ ) and diffusion-controlled process ( $k_2\nu^{1/2}$ ) at a fixed potential ( $V$ ),<sup>34,35</sup> according to the relation:

$$i(V) = k_1\nu + k_2\nu^{1/2} \quad (4)$$

where  $k_1$  and  $k_2$  are constants. Based on the quantification, 81.7% of the total charge was contributed by the capacitive

process at a scan rate of  $0.5 \text{ mV s}^{-1}$  (Fig. S11c†). Even at a slow scan rate of  $0.1 \text{ mV s}^{-1}$  with the diffusion-controlled contribution at the maximum, the capacitive contribution ratio still accounted for 75.6%, as shown in Fig. S11d.† Also, together with the increase in the scan rate, the capacitive contribution increased continuously. The above electrochemical behaviors suggest that the charge-storage mechanism of the tungstate fiber electrode should be governed by an intercalation pseudocapacitive process,<sup>15,33</sup> which is the result of the 2D nanofluidic channels and 3D interconnected tunnels for exclusive and fast ion transport.

The flexibility of the fiber-shaped LIBs was also investigated. Fig. 3d shows the galvanostatic charge/discharge curves of the fiber battery under different bending states, including before bending and at bending angles ( $\theta$ ) of  $90^\circ$ ,  $120^\circ$ , and  $150^\circ$  during the test procedure. Even under very high bending angles, the galvanostatic charge/discharge curves remained almost unchanged and over 91% reversible capacity remained compared to that before bending. The fiber battery also exhibited an excellent bending cycling performance, as shown in Fig. 3e, giving the capacity retention of about 77% and CE of  $\sim 100\%$  after 200 bending cycles. Meanwhile, the fiber showed no obvious structure cracks under SEM observation after the bending cycles (Fig. S12†). Furthermore, even after 200 repeated bending cycles, the capacity retention was still maintained above 72.2% (Fig. S13†). These results demonstrate the high flexibility and stability of the fiber battery, which is comparable to that reported for fiber-shaped LIBs (Table S1†). As an application demonstration, the fiber batteries were woven into a Chinese knot in parallel, which could power three commercial green light-emitting diodes (LEDs) connected in series (Fig. 3f and Movie S1†). Also, under the dynamic bending process with various bending angles, the illumination intensity of the LED remained constant, as shown in Fig. 3g and Movie S2.† Moreover, the voltage outputs of the fiber battery also exhibited no significant change under the straight and bending states, which gave a stable voltage of 3.1 V even though the fiber battery was bent up to  $180^\circ$  (Fig. 3h and S14†). Benefiting from the excellent flexibility contributed from the aligned stacking structures of the nanosheets, the fiber-shaped LIBs promise high application value in wearable devices.

## Fiber-shaped sodium ion battery

Considering their similar energy storage mechanism as LIBs, fiber-shaped SIBs were fabricated by employing the same strategies and technologies. Although the large ion radius and heavy mass of sodium will slow down the ionic transport more seriously,<sup>36–38</sup> the tungstate/rGO fiber possibly provides a new opportunity to improve the sluggish kinetics for  $\text{Na}^+$  intercalation. As shown in Fig. S15,† the galvanostatic charge/discharge curves for the 1st, 2nd, 5th, and 10th cycles were collected at 0.052 mA with a fiber length of 8 cm. The initial charge and discharge capacities were 182.8 and 225.1  $\text{mA h g}^{-1}$ , respectively. The corresponding CE was calculated to 81.2%, this loss of reversible capacity can be attributed to the formation of an SEI layer. During the subsequent cycles, the charge/discharge

curves mainly overlapped and exhibited continuous capacity changes without an obvious voltage plateau, similar to the fast charge-storage kinetics governed by the capacitive process in the fiber-shaped LIBs. At the end of the 10th cycle, the reversible capacity remained at  $178.6 \text{ mA h g}^{-1}$  with a CE of  $\sim 100\%$ , suggesting the excellent reversibility of the fiber during the  $\text{Na}^+$  intercalation processes. Fig. 4a and b display the rate capability of the fiber battery under various currents ranging from 0.052 mA to 0.520 mA. The reversible capacity declined steadily with an increase in current and could recover to its initial value with a CE of  $\sim 100\%$  when the current decreased to 0.052 mA again. This excellent rate capability is comparable to that of the fiber-shaped LIBs, demonstrating that the fiber also possesses favorable ionic transport properties for  $\text{Na}^+$  intercalation. Moreover, the long-term cycling performance of the fiber battery is shown in Fig. 4c. After 1000 cycles, the reversible capacity was still maintained at  $106.1 \text{ mA h g}^{-1}$  under the current of 0.520 mA. The corresponding CE was  $\sim 100\%$  and the average capacity decay was less than 0.0184% per cycle, which surpasses that for pure tungstate (Fig. S16†). These superior electrochemical performances should also be attributed to the interstratified stacking structures of the tungstate and graphene, which could provide 2D nanofluidic channels and 3D interconnected tunnels for efficient ion transport, and excellent conductive networks of conformal stacking graphene. As shown in the Nyquist plots (Fig. S17†), the  $R_s$  value was about 97.5  $\Omega$ , which decreased to about 67.6  $\Omega$  after 100 cycles; meanwhile, the  $R_{ct}$  value was about 317.6  $\Omega$  and decreased to about 203.9  $\Omega$  after 100 cycles. Similarly, the slope of the straight line in the low-frequency zone also showed the low Warburg impedance and acceptable ion diffusion in the fiber. The slight difference in the Nyquist plots between the LIB and SIB should be caused by the large ion radius and heavier mass of the sodium ions.

The charge-storage kinetics for  $\text{Na}^+$  intercalation was also investigated *via* a CV experiment. As shown in Fig. S18a,† the CV curves at various scan rates ranging from 0.1 to  $0.9 \text{ mV s}^{-1}$  display similar shapes with small peak separations in the anodic and cathodic processes. According to the power-law relationship between peak current and scan rate, as shown in eqn (3), the  $b$ -values for both the anodic and cathodic peaks were quantified to be about 0.87 and 0.85, respectively, suggesting the features of intercalation pseudocapacitive behaviors (Fig. 4d). Moreover, the capacitive contribution could be quantitated by separating the current response from the capacitive and diffusion-controlled processes based on eqn (4). As shown in Fig. S18b,† the capacitive process contributed almost 74.6% of the total storage charge at  $0.5 \text{ mV s}^{-1}$ . With an increase in the scan rate increase, the percentage capacitive contribution increased, and a high value of 82.1% was achieved at  $0.9 \text{ mV s}^{-1}$  (Fig. 4e). These results demonstrate that the charge-storage mechanism for  $\text{Na}^+$  is also dominated by the intercalation pseudocapacitive process and the strategy of improving the ion transport properties of fiber electrodes by engineering 2D nanofluidic channels and 3D interconnected ion transport tunnels is feasible.

The flexibility of the fiber-shaped SIBs was also evaluated *via* a galvanostatic charge/discharge experiment. As shown in

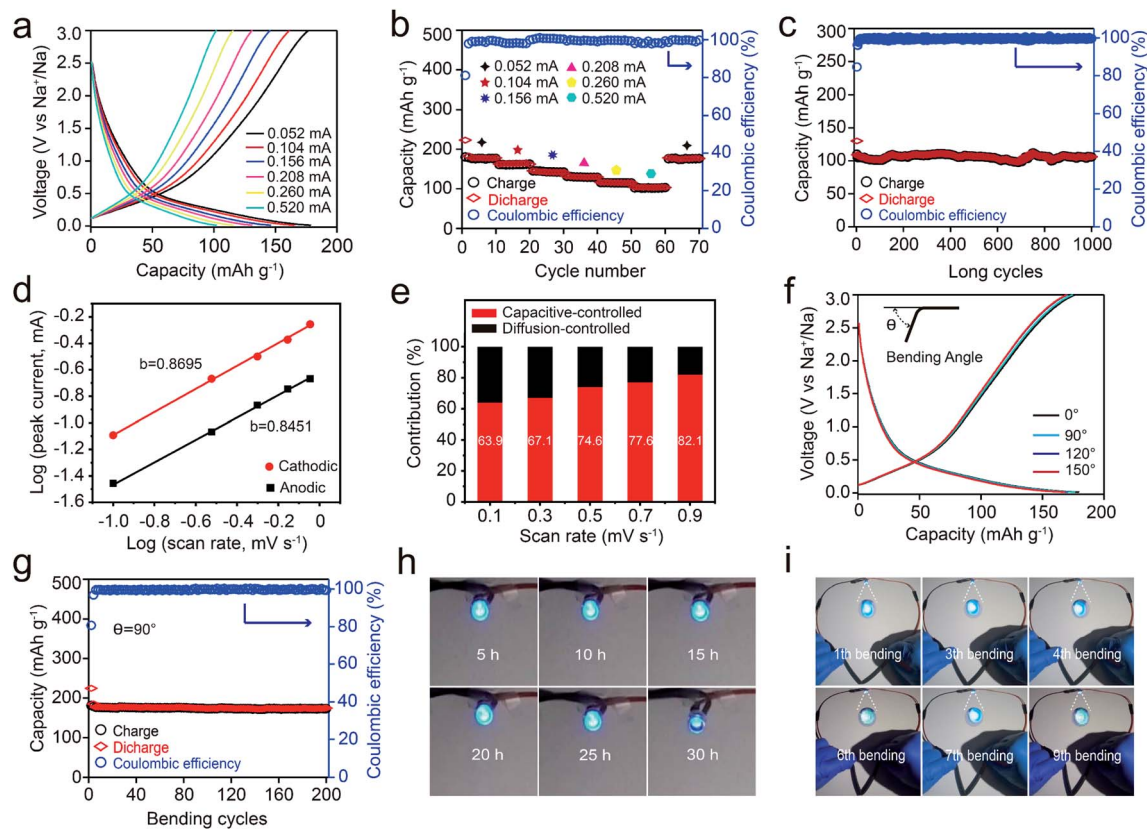


Fig. 4 Electrochemical performance of the fiber-shaped SIBs. (a) Galvanostatic charge/discharge profiles of the fiber battery under different currents ranging from 0.052 mA to 0.520 mA. (b) Rate capability of the fiber battery under different currents ranging from 0.052 mA to 0.520 mA. (c) Cycling performance and corresponding coulombic efficiency of the fiber battery at 0.520 mA. (d) Determination of the  $b$ -value by utilizing the power-law relationship between peak current and scan rate. (e) Contribution ratio of capacitive-controlled (red) and diffusion-controlled (black) capacities at different scan rates. (f) Galvanostatic charge/discharge curves of the fiber battery under different bending angles at 0.052 mA. (g) Bending cycling performance of the fiber battery under a bending angle of  $90^\circ$  at 0.052 mA. (h) Photographs of the fiber battery lighting a blue LED under repeated bending. (i) Fiber battery continuously lighting a blue LED for more than 30 h.

Fig. 4f, almost no changes in the charge/discharge curves were detected before and after mechanical bending. The corresponding capacity retention still remained above 93.7% even under a bending angle of  $150^\circ$ , indicating that the fiber battery exhibited high tolerability to mechanical deformations. Fig. 4g shows the bending cycling performance of the fiber battery under the bending angle of  $90^\circ$ . After 200 bending cycles, the reversible capacity remained above 77.8% with a CE of  $\sim 100\%$ , and the fiber also exhibited no visible cracks under SEM observation (Fig. S19<sup>†</sup>). Moreover, even after 200 repeated bending cycles, a high capacity retention of 71.3% was maintained (Fig. S20<sup>†</sup>). These results prove the high flexibility and stability of the fiber battery, which are also comparable to that reported for fiber-shaped SIBs (Table S1<sup>†</sup>). To verify its practicability, the fiber battery was employed to power a commercial LED. Owing to its excellent charge-storage performance, a single fiber battery with a length of 8 cm could continuously power the LED for more than 30 h (Fig. 4h). Even under repeated mechanical bending, the illumination intensity of the LED exhibited no decay (Fig. 4i and Movie S3<sup>†</sup>), indicating the promising prospects of the fiber battery in practical applications.

## Discussion

The above superior flexibility and electrochemical performances of the tungstate/rGO fiber for both fiber-shaped LIBs and SIBs should be associated with the following advantages: (1) fast and efficient charge storage contributed from the intercalation pseudocapacitive process. The tungstate nanosheets possess a rigid and open host lattice (inset in Scheme 1b), which is the structural characteristic necessary for intercalation pseudocapacitance, offering 3D interconnected hexagonal tunnels of W–O chains as transport pathways and avoiding the intercalation ions from being trapped. The charge storage could achieve a high level within a short period of time, and thus not limited by solid-state diffusion and phase transformations due to the structural change upon intercalation. (2) Shortened ion diffusion distance and extra charge storage sites provided by the ultrathin 2D structure. With the ultrathin thickness of about 2 nm, the tungstate nanosheets exhibit large exposed surfaces similar to other typical 2D nanomaterials, providing abundant electrochemically active sites and shortened diffusion distances for ion diffusion and intercalation. (3) Minimum ion-path tortuosity and exclusive ion transport

enabled by 2D nanofluidic channels. The aligned stacking structures within the fiber can greatly reduce the ion-path tortuosity, providing a shorter diffusion pathway for lithium and sodium ions across the fiber electrode. More importantly, through the cooperation of stacked spacing (comparable to double-Debye length) and negative surface charge of the nanosheets, 2D nanofluidic channels can be achieved, as shown in Scheme 1b. Inside the narrow channels, electrostatic effects can persist, which will repel ions of negative charge and attract the positive lithium and sodium ions, making them the charge carriers. This exclusive ion transport behavior can enhance the ionic conductivity up to several orders of magnitude, ultimately improving the battery performance. (4) Excellent flexible backbone and conductive networks as a result of interstratified stacking structures. Benefiting from the molecular hybridization and conformal stacking of the tungstate and rGO nanosheets, the interstratified stacking structures can endow the fiber with good structural resistance to mechanical deformation and electrical conductivity, which ensure its suitability for serving as a flexible fiber electrode.

In summary, tungstate/rGO fibers were successfully spun from a mixed 2D LC colloid *via* the wet-spinning technique. Benefitting from the constructed 2D nanofluidic channels, 3D interconnected ion transport tunnels, and excellent flexible backbone and conductive networks of the conformal stacking graphene and tungstate nanosheets, the fiber electrode exhibited accelerated ion transport behaviors, efficient charge storage governed by the intercalation pseudocapacitive process and sufficient resistance to mechanical deformations. To demonstrating the electrochemical applications of the tungstate/rGO fiber, fiber-shaped LIBs and SIBs were fabricated, which exhibited a high capacity (206 and 178 mA h g<sup>-1</sup> at 0.052 mA with a fiber length of 8 cm, respectively), excellent rate performance, long-term cycling capability (1000 cycles), and outstanding flexibility (200 bending cycles and continuously lighting an LED under mechanical bending). Thus, the strategy proposed herein for the structural engineering of fiber electrodes provides a promising way to improve the overall performance of fiber batteries, facilitating their further development in practical wearable applications.

## Conflicts of interest

The authors declare no competing interests.

## Acknowledgements

This work was supported by the National Natural Science Foundation of China (No. 51572058, 51761135123, 51702068), National Key Research & Development Program (2016YFB0303903, 2016YFE0201600), the International Science & Technology Cooperation Program of China (2013DFR10630, 2015DFE52770), and Foundation of Equipment Development Department (6220914010901).

## References

- 1 H. Sun, Y. Zhang, J. Zhang, X. M. Sun and H. S. Peng, *Nat. Rev. Mater.*, 2017, **2**, 17023.
- 2 Y. H. Zhu, X. Y. Yang, T. Liu and X. B. Zhang, *Adv. Mater.*, 2019, 1901961.
- 3 X. Xu, S. Xie, Y. Zhang and H. Peng, *Angew. Chem., Int. Ed.*, 2019, **58**, 13643–13653.
- 4 F. Mo, G. Liang, Z. Huang, H. Li, D. Wang and C. Zhi, *Adv. Mater.*, 2019, 1902151.
- 5 L. Wang, X. Fu, J. He, X. Shi, T. Chen, P. Chen, B. Wang and H. Peng, *Adv. Mater.*, 2019, 1901971.
- 6 Y. Zhou, C. H. Wang, W. Lu and L. Dai, *Adv. Mater.*, 2019, 1902779.
- 7 M. Tebyetekerwa, I. Marriam, Z. Xu, S. Y. Yang, H. Zhang, F. Zabihi, R. Jose, S. J. Peng, M. F. Zhu and S. Ramakrishna, *Energy Environ. Sci.*, 2019, **12**, 2148–2160.
- 8 W. Liu, M. S. Song, B. Kong and Y. Cui, *Adv. Mater.*, 2017, **29**, 1603436.
- 9 Z. X. Liu, F. N. Mo, H. F. Li, M. S. Zhu, Z. F. Wang, G. J. Liang and C. Y. Zhi, *Small Methods*, 2018, **2**, 1800124.
- 10 C. J. Zhang, J. X. Zhu, H. J. Lin and W. Huang, *Adv. Mater. Technol.*, 2018, **3**, 1700302.
- 11 L. J. Lu, Y. J. Hu and K. Dai, *Mater. Today Chem.*, 2017, **5**, 24–33.
- 12 Y. Y. Liu, Y. Y. Zhu and Y. Cui, *Nat. Energy*, 2019, **4**, 540–550.
- 13 J. Liu, J. Wang, C. Xu, H. Jiang, C. Li, L. Zhang, J. Lin and Z. X. Shen, *Adv. Sci.*, 2018, **5**, 1700322.
- 14 M. Liao, L. Ye, Y. Zhang, T. Chen and H. Peng, *Adv. Electron. Mater.*, 2019, **5**, 1800456.
- 15 M. R. Lukatskaya, B. Dunn and Y. Gogotsi, *Nat. Commun.*, 2016, **7**, 12647.
- 16 K. J. Griffith, K. M. Wiaderek, G. Cibin, L. E. Marbella and C. P. Grey, *Nature*, 2018, **559**, 556–563.
- 17 T. Brezesinski, J. Wang, S. H. Tolbert and B. Dunn, *Nat. Mater.*, 2010, **9**, 146–151.
- 18 Y. Xia, T. S. Mathis, M. Q. Zhao, B. Anasori, A. Dang, Z. Zhou, H. Cho, Y. Gogotsi and S. Yang, *Nature*, 2018, **557**, 409–412.
- 19 J. Billaud, F. Bouville, T. Magrini, C. Villevieille and A. R. Studart, *Nat. Energy*, 2016, **1**, 1–6.
- 20 B. Mendoza-Sanchez and Y. Gogotsi, *Adv. Mater.*, 2016, **28**, 6104–6135.
- 21 K. Fukuda, K. Akatsuka, Y. Ebina, R. Ma, K. Takada, I. Nakai and T. Sasaki, *ACS Nano*, 2008, **2**, 1689–1695.
- 22 R. Ma and T. Sasaki, *Adv. Mater.*, 2010, **22**, 5082–5104.
- 23 P. Xiong, R. Ma, N. Sakai and T. Sasaki, *ACS Nano*, 2018, **12**, 1768–1777.
- 24 P. Xiong, B. Sun, N. Sakai, R. Ma, T. Sasaki, S. Wang, J. Zhang and G. Wang, *Adv. Mater.*, 2019, 1902654.
- 25 Z. Xu and C. Gao, *Nat. Commun.*, 2011, **2**, 571.
- 26 Y. Liu, Z. Xu, W. Gao, Z. Cheng and C. Gao, *Adv. Mater.*, 2017, **29**, 1606794.
- 27 A. R. Koltonow and J. Huang, *Science*, 2016, **351**(6280), 1395–1396.
- 28 Y. Zhu, L. Peng, Z. Fang, C. Yan, X. Zhang and G. Yu, *Adv. Mater.*, 2018, **30**, 1706347.
- 29 C. Yan, C. Lv, Y. Zhu, G. Chen, J. Sun and G. Yu, *Adv. Mater.*, 2017, **29**, 1703909.

- 30 Z. Xu and C. Gao, *ACS Nano*, 2011, **5**, 2908–2915.
- 31 D. Stein, M. Kruithof and C. Dekker, *Phys. Rev. Lett.*, 2004, **93**, 035901.
- 32 R. B. Schoch, J. Han and P. Renaud, *Rev. Mod. Phys.*, 2008, **80**, 839–883.
- 33 V. Augustyn, J. Come, M. A. Lowe, J. W. Kim, P. L. Taberna, S. H. Tolbert, H. D. Abruna, P. Simon and B. Dunn, *Nat. Mater.*, 2013, **12**, 518–522.
- 34 V. Augustyn, P. Simon and B. Dunn, *Energy Environ. Sci.*, 2014, **7**, 1597–1614.
- 35 D. Chao, C. Zhu, P. Yang, X. Xia, J. Liu, J. Wang, X. Fan, S. V. Savilov, J. Lin, H. J. Fan and Z. X. Shen, *Nat. Commun.*, 2016, **7**, 12122.
- 36 L. W. Peng Gao, Y. Zhang, Y. Huang and K. Liu, *ACS Nano*, 2015, **9**, 11296–11301.
- 37 Z. Li, X. Mu, Z. Zhao-Karger, T. Diemant, R. J. Behm, C. Kubel and M. Fichtner, *Nat. Commun.*, 2018, **9**, 5115.
- 38 D. Han, J. Zhang, Z. Weng, D. Kong, Y. Tao, F. Ding, D. Ruan and Q.-H. Yang, *Materials Today Energy*, 2019, **11**, 30–45.